Fingering stabilization and adhesion force in the lifting flow with a fluid annulus

Írio M. Coutinho [1,*] Pedro H. A. Anjos [2,†] Rafael M. Oliveira [2,‡] and José A. Miranda [1,§]
[1]*Departamento de Física, Universidade Federal de Pernambuco, CCEN, Recife, Pernambuco 50670-901, Brazil*
[2]*Departamento de Engenharia Mecânica, Pontifícia Universidade Católica do Rio de Janeiro, Rio de Janeiro 22451-900, Brazil*

(Received 10 October 2023; accepted 4 January 2024; published 23 January 2024)

The lifting Hele-Shaw cell flow commonly involves the stretching of a viscous oil droplet surrounded by air, in the confined space between two parallel plates. As the upper plate is lifted, viscous fingering instabilities emerge at the air-oil interface. Such an interfacial instability phenomenon is widely observed in numerous technological and industrial applications, being quite difficult to control. Motivated by the recent interest in controlling and stabilizing the Saffman-Taylor instability in lifting Hele-Shaw flows, we propose an alternative way to restrain the development of interfacial disturbances in this gap-variable system. Our method modifies the traditional plate-lifting flow arrangement by introducing a finite fluid annulus layer encircling the central oil droplet, and separating it from the air. A second-order, perturbative mode-coupling approach is employed to analyze morphological and stability behaviors in this three-fluid, two-interface, doubly connected system. Our findings indicate that the intermediate fluid ring can significantly stabilize the interface of the central oil droplet. We show that the effectiveness of this stabilization protocol relies on the appropriate choice of the ring's viscosity and thickness. Furthermore, we calculate the adhesion force required to detach the plates, and find that it does not change significantly with the addition of the fluid envelope as long as it is sufficiently thin. Finally, we detect no distinction in the adhesion force computed for stable or unstable annular interfaces, indicating that the presence of fingering at the ring's boundaries has a negligible effect on the adhesion force.

DOI: 10.1103/PhysRevE.109.015104

I. INTRODUCTION

The Saffman-Taylor (or viscous fingering) instability [1] is a popular fluid dynamic problem that takes place in the confined geometry of Hele-Shaw cells (two motionless glass plates separated by a small gap) when a less viscous fluid is injected against a more viscous one. The viscosity difference between the fluids makes the two-fluid interface unstable, resulting in the formation of complex patterns, where multiple fingerlike structures are formed [2–7]. This iconic interfacial instability has been the object of considerable interest since the late 1950s, mostly due to its multiple scientific and practical applications, and since then has become a paradigmatic system for interfacial instabilities and pattern formation [8].

A variant of the traditional injection-driven, viscous fingering situation in motionless-plates Hele-Shaw cells, is the lifting Hele-Shaw cell problem [9–13]. In this alternative setting, a more viscous fluid droplet surrounded by a less viscous fluid is stretched, when the upper cell plate is lifted uniformly, and the lower plate remains at rest. In contrast to the conventional injection-induced, fixed-gap arrangement, in the lifting version the cell gap varies with time. During the lifting-plate process, the outer less viscous fluid penetrates the more viscous central droplet, and the contracting fluid-fluid interface quickly deforms as it moves inwards toward the center of the cell. As a result, visually striking interfacial patterns arise [14–16], which are very different from those produced in the injection-induced, constant-gap configuration. Regarding important technological applications, it is worth noting that the lifting Hele-Shaw cell problem involves essentially the same setup as the one utilized in the so-called probe-tack test [17–19], an experimental technique widely used to study technologically relevant problems in adhesion science [20–25].

Despite the richness of the pattern formation systems associated with the Saffman-Taylor instability, and its scientific and practical relevance, depending on the situation the development of interfacial instabilities can be undesirable, and difficult to control. For example, the viscous fingering instability is a major cause of poor oil recovery [26,27], once evolving branching fingers may reach the entrance of the well, and mainly water, and not petroleum is retrieved. A similar unwelcome effect occurs during displacement of groundwater by hydrogen [28,29] in renewable energy processes, where the viscous fingering instability leads to gas leakage from anticlinal traps and stimulates undesired gas dissolution. Furthermore, the development of viscous fingering is potentially detrimental to chromatographic separation processes [30,31] and can also be unwanted in applications involving adhesives [21–25] and in the fabrication of lithium rechargeable batteries [32,33]. In this way, it is of great importance to find ways to minimize, suppress, and control the growth of interfacial disturbances in these systems.

Several strategies have been pursued to restrain and possibly stabilize the growth of fingering patterns in injection-driven, radial Hele-Shaw cells with motionless plates. To obtain the desired stabilization, researchers modified the geometry of the Hele-Shaw cell, through the

*irio.menezes@ufpe.br
†pamorimanjos@esp.puc-rio.br
‡rmo@puc-rio.br
§jose.mirandant@ufpe.br

use of elastic [34–36] and tapered [37–39] plates, employed various different fluid injection schemes [40–46], added suspended particles at the fluid-fluid interface [47,48], and utilized applied external electric fields [49–51].

A relatively smaller number of studies have been devoted to try to control and eventually stabilize fingering instabilities occurring in confined lifting flows. Recently, an interesting experimental investigation in a lifting Hele-Shaw cell with a modified geometry has shown that it is possible to generate more regular meshlike patterns in such gap-variable circumstances by introducing holes in the cell plates in a setup named the "multiport lifted Hele-Shaw cell" [52]. A related theoretical study [53] used linear stability analysis and numerical simulations to analyze a simplified version of the multiport arrangement proposed in Ref. [52], and considered a lifting Hele-Shaw cell with a single hole in the upper cell plate. The existence of such a single hole makes the less viscous outer fluid to penetrate the confined more viscous liquid simultaneously from two fronts: the periphery and from the center of the cell. In this two-interface scenario, the authors of Ref. [53] characterized the stability of the invading fingers and demarcated parameter regions over which the resulting interfaces are unstable.

Even more recently, investigators performed probe-tack adhesion measurements of viscoelastic thin films in a modified version of the lifting Hele-Shaw cell [54]. In Ref. [54] the rigid upper plate of the lifting apparatus is replaced by a soft spherical probe. Under these conditions, they examined how the mode of debonding between the soft probe and the viscoelastic adhesive film is impacted as the compliance of the probe is varied. Their experimental results demonstrate that the adhesive-air interface stabilizes as the compliance of the probe is increased [see Figs. 1(c)–1(e) in Ref. [54]]. In other words, they have found that detachment from a soft probe suppresses the Saffman-Taylor instabilities normally encountered in probe-tack adhesion experiments with rigid probes (for many examples of such unstable patterns, see Refs. [13–15,20,21]). In addition, they have also verified that the adhesion strength (i.e., the maximum value of the adhesion force) is nearly the same for stable and unstable adhesive-air interfaces (see Fig. 2 in Ref. [54]).

Motivated by the recent interest in controlling and stabilizing the Saffman-Taylor instability in lifting Hele-Shaw flows [52–54], and stimulated by the related findings of Ref. [54] concerning the impact of fingering on the adhesive strength, in this paper we propose an alternative way to control interfacial disturbances in this gap-variable fluid flow system. More precisely, we investigate the possibility of stabilizing a shrinking interface separating a central droplet of a viscous fluid (e.g., oil), originally surrounded by a fluid of negligible viscosity (e.g., air). Note that this particular setup (single oil-air interface) is precisely the most common situation studied in many existing theoretical and experimental research explorations of lifting Hele-Shaw flows and fluid adhesion problems (see, for example, Refs. [9–16,20–25]). We seek interface stabilization (see Fig. 1) by enveloping the central droplet (fluid 1) with a fluid annulus of intermediate viscosity (fluid 2) between those of fluids 1 and the outmost fluid (fluid 3). In this framing, in addition to examining the stability behavior of the inner and outer interfaces of the intermediate annular fluid ring, we also evaluate the influence of the fluid annular structure on the adhesion force in such a modified lifting Hele-Shaw flow configuration.

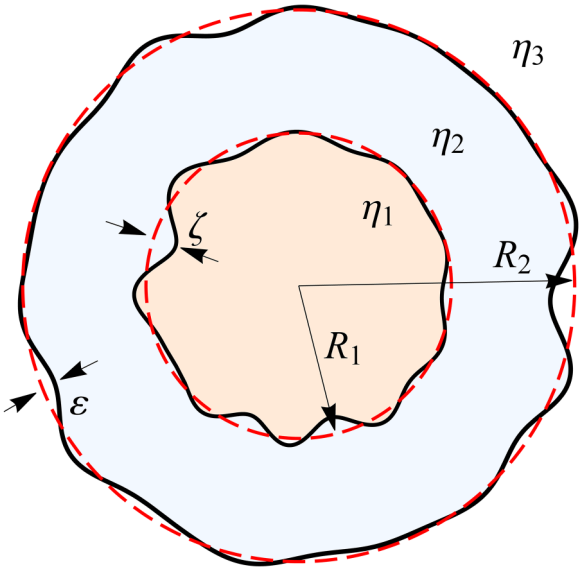

FIG. 1. Schematic illustration (upper view) of the time-dependent gap $[b = b(t)]$, or lifting flow in a Hele-Shaw cell containing three fluids. A fluid annulus of viscosity η_2 surrounds a central droplet of viscosity η_1 and separates this region from an infinite fluid domain of negligible viscosity $\eta_3 \ll \eta_1, \eta_2$. Between fluids 1 and 2 (2 and 3), there exists a perturbed interface (solid curve) represented by $\mathcal{R}_1(\theta, t) = R_1(t) + \zeta(\theta, t)$ $[\mathcal{R}_2(\theta, t) = R_2(t) + \varepsilon(\theta, t)]$, where $\zeta(\theta, t)$ $[\varepsilon(\theta, t)]$ is a small interfacial perturbation. Additionally, the dashed circle with radius $R_1(t)$ $[R_2(t)]$ expresses the time-dependent unperturbed inner (outer) boundary of the annular structure.

The outline of the rest of the paper is as follows. In Sec. II we formulate the physical problem and present the governing equations used to model the motion of the fluid annulus. By employing a second-order, perturbative mode-coupling approach, we derive a set of coupled nonlinear differential equations which describes the time evolution of the inner and outer interfaces of the fluid ring. In Sec. III we analyze some relevant features of the pattern formation dynamics and interfacial stabilization in the early nonlinear regime. We focus on understanding how the viscosity and thickness of the intermediate fluid ring affect the development and stability of the nonlinear pattern-forming annular structures. Then, in Sec. IV, we derive the fluid adhesion force considering the presence of the fluid annulus, as well as the fingering formation on its boundaries. Under these circumstances, we examine how the ring's viscosity and thickness influence the adhesion force as time advances. Finally, Sec. V summarizes our main results and presents some concluding remarks.

II. PROBLEM FORMULATION AND GOVERNING EQUATIONS

Figure 1 illustrates the physical system considered in this paper, a Hele-Shaw cell of variable gap thickness b (as seen from above). In such an apparatus, while the lower plate of the cell is kept fixed, the upper glass plate is lifted along the

direction perpendicular to the cell plates, and thus, the gap thickness varies in time [$b = b(t)$]. As the upper plate moves upward with lifting velocity $\dot{b} = db/dt$, three fluids with viscosities denoted by η_1, η_2, and η_3 flow within the Hele-Shaw cell toward its center. Fluid 1 forms the central droplet enveloped by an annular-shaped region of fluid 2. Surrounding both of these fluids there is an infinite fluid domain composed of fluid 3. The fluids are immiscible, incompressible, and Newtonian.

At the beginning of the lifting flow process ($t = 0$), a nearly circular interface having surface tension σ_{12}, and located at the radial distance $R_1(t = 0) = R_1(0)$ (represented by the inner dashed circle in Fig. 1) separates fluids 1 and 2. Likewise, a second interface having surface tension σ_{23} at $R_2(t = 0) = R_2(0)$ (represented by the outer dashed circle in Fig. 1) separates fluids 2 and 3. As the upper plate starts to move upwards, the slightly perturbed, circular interfaces can become unstable and deform, due to the action of the Saffman-Taylor instability. These perturbed boundaries (depicted as the inner and outer solid lines in Fig. 1) are mathematically described as $\mathcal{R}_1(\theta, t) = R_1(t) + \zeta(\theta, t)$ and $\mathcal{R}_2(\theta, t) = R_2(t) + \varepsilon(\theta, t)$, where θ denotes the azimuthal angle and

$$\zeta(\theta, t) = \sum_{n=-\infty}^{+\infty} \zeta_n(t)\, e^{in\theta} \tag{1}$$

and

$$\varepsilon(\theta, t) = \sum_{n=-\infty}^{+\infty} \varepsilon_n(t)\, e^{in\theta} \tag{2}$$

are the netinterface perturbations on the inner and outer boundaries, respectively. In the Fourier expansions (1) and (2), $\zeta_n(t)$ and $\varepsilon_n(t)$ represent complex Fourier amplitudes with integer wave numbers n. In addition, we include the $n = 0$ mode in the summations to maintain the area of the regions filled with fluids 1 and 2 independent of the net perturbations [4], leading to the relations $\zeta_0 = -\frac{1}{2R_1}\sum_{n=1}^{\infty}[|\zeta_n(t)|^2 + |\zeta_{-n}(t)|^2]$, and $\varepsilon_0 = -\frac{1}{2R_2}\sum_{n=1}^{\infty}[|\varepsilon_n(t)|^2 + |\varepsilon_{-n}(t)|^2]$ [55]. Furthermore, volume conservation imposes that the unperturbed radii vary in time according to the equations

$$R_1(t) = R_1(0)\sqrt{\frac{b_0}{b(t)}} \tag{3}$$

and

$$R_2(t) = R_2(0)\sqrt{\frac{b_0}{b(t)}}, \tag{4}$$

where $b(t = 0) = b_0$.

In our theoretical description of the plate-lifting Hele-Shaw flow, the lifting velocity $\dot{b}$ must be small, allowing us to neglect inertial effects safely. Moreover, despite the increasing values of b over time due to the lifting procedure, it is also necessary to ensure that the system always remains at a large aspect ratio, i.e., $b(t) \ll R_1(t), R_2(t)$. As it will become clear in Sec. III, such requirements are easily met by the appropriate choice of physical parameters. Under these circumstances, the quasi-two-dimensional flow that takes place within the Hele-Shaw setting can be described by the gap-averaged Darcy's law [1,8]

$$\mathbf{v}_j = -\frac{b^2(t)}{12\eta_j}\nabla p_j \tag{5}$$

and by a modified gap-averaged incompressibility condition [9,13]

$$\nabla \cdot \mathbf{v}_j = -\frac{\dot{b}(t)}{b(t)}, \tag{6}$$

where $\mathbf{v}_j = \mathbf{v}_j(r, \theta)$ and $p_j = p_j(r, \theta)$ represent the gap-averaged velocity and pressure in fluid j (with $j = 1, 2$, or 3), respectively, and r denotes the radial coordinate.

Besides the governing equations (5) and (6), we need two sets of boundary conditions at each fluid-fluid interface in order to determine the interfacial motions. For the innermost interface located between fluid layers 1 and 2, the first set of conditions is given by the Young-Laplace pressure jump boundary condition [1,8] due to the surface tension σ_{12}, and by the kinematic boundary condition [8], which states that the normal components of each fluid's velocity are continuous across the inner interface. These are respectively given by

$$(p_1 - p_2)|_{r=\mathcal{R}_1} = \sigma_{12}\kappa_{12}|_{r=\mathcal{R}_1} \tag{7}$$

and

$$(\mathbf{v}_1 \cdot \hat{\mathbf{n}})|_{r=\mathcal{R}_1} = (\mathbf{v}_2 \cdot \hat{\mathbf{n}})|_{r=\mathcal{R}_1}. \tag{8}$$

Similarly, the second set of boundary conditions acting on the outermost interface is

$$(p_2 - p_3)|_{r=\mathcal{R}_2} = \sigma_{23}\kappa_{23}|_{r=\mathcal{R}_2} \tag{9}$$

and

$$(\mathbf{v}_2 \cdot \hat{\mathbf{n}})|_{r=\mathcal{R}_2} = (\mathbf{v}_3 \cdot \hat{\mathbf{n}})|_{r=\mathcal{R}_2}. \tag{10}$$

Note that in Eqs. (7) and (9), κ_{12} and κ_{23} denote the interfacial curvatures on the plane of the cell for the inner and outer interfaces, respectively. Additionally, $\hat{\mathbf{n}}$ appearing in Eqs. (8) and (10) is the unit normal vector at the interfaces.

As the flow field is irrotational in the bulk of each fluid, i.e., $\nabla \times \mathbf{v}_j = 0$, it allows the definition of velocity potentials ϕ_j, with $\mathbf{v}_j = -\nabla\phi_j$. By taking into account the modified incompressibility condition (6), one can find that these velocity potentials satisfy Poisson's equation $\nabla^2\phi_j = \dot{b}(t)/b(t)$, with general solution (for $j = 1, 2, 3$)

$$\phi_1(r, \theta) = \frac{\dot{b}r^2}{4b} + \sum_n \alpha_n(t)\left(\frac{r}{R_1}\right)^{|n|} e^{in\theta}, \tag{11}$$

$$\phi_2(r, \theta) = \frac{\dot{b}r^2}{4b} + \sum_n \beta_n(t)\left(\frac{r}{R_1}\right)^{-|n|} e^{in\theta} + \sum_n \gamma_n(t)\left(\frac{r}{R_2}\right)^{|n|} e^{in\theta}, \tag{12}$$

$$\phi_3(r, \theta) = \frac{\dot{b}r^2}{4b} + \sum_n \omega_n(t)\left(\frac{r}{R_2}\right)^{-|n|} e^{in\theta}. \tag{13}$$

We seek to describe the motion and shape of the two interfaces present in our annular system by means of a mode-coupling, weakly nonlinear theory accurate to second order in the perturbation amplitudes ζ_n and ε_n [4,55,56]. This is

accomplished by first restating the problem in terms of ϕ_j, and then relating these velocity potentials (11)–(13) to ζ_n and ε_n through the kinematic boundary conditions (8) and (10). These newly found relations are then plugged in together with the remaining Young-Laplace conditions (7) and (9) into Darcy's law (5). By keeping only terms up to second order in ζ_n and ε_n, we obtain, after Fourier transforming, the set of coupled equations of motion for both the perturbation amplitudes ζ_n and ε_n (for $n \neq 0$)

$$\begin{aligned}\dot{\zeta}_n = {} & f_1\,\Lambda(n)\zeta_n + f_2\,\Gamma(n)\varepsilon_n \\ & + f_1 \sum_{p\neq 0}[F(n,p)\zeta_p\zeta_{n-p} + G(n,p)\dot{\zeta}_p\zeta_{n-p}] \\ & + f_2 \sum_{p\neq 0}[H(n,p)\varepsilon_p\varepsilon_{n-p} + I(n,p)\dot{\varepsilon}_p\varepsilon_{n-p}] \\ & + f_2 \sum_{p\neq 0}[J(n,p)\varepsilon_p\zeta_{n-p} + K(n,p)\dot{\varepsilon}_p\zeta_{n-p} \\ & + L(n,p)\zeta_p\varepsilon_{n-p} + M(n,p)\dot{\zeta}_p\varepsilon_{n-p}] \end{aligned} \tag{14}$$

and

$$\begin{aligned}\dot{\varepsilon}_n = {} & f_3\,\Omega(n)\zeta_n + f_4\,\Xi(n)\varepsilon_n \\ & + f_3 \sum_{p\neq 0}[\mathcal{F}(n,p)\zeta_p\zeta_{n-p} + \mathcal{G}(n,p)\dot{\zeta}_p\zeta_{n-p}] \\ & + f_4 \sum_{p\neq 0}[\mathcal{H}(n,p)\varepsilon_p\varepsilon_{n-p} + \mathcal{I}(n,p)\dot{\varepsilon}_p\varepsilon_{n-p}] \\ & + f_3 \sum_{p\neq 0}[\mathcal{J}(n,p)\varepsilon_p\zeta_{n-p} + \mathcal{K}(n,p)\dot{\varepsilon}_p\zeta_{n-p} \\ & + \mathcal{L}(n,p)\zeta_p\varepsilon_{n-p} + \mathcal{M}(n,p)\dot{\zeta}_p\varepsilon_{n-p}], \end{aligned} \tag{15}$$

where

$$\Lambda(n) = -\frac{\dot{b}}{2b}\left(|n| + f_1^{-1}\right) - \frac{b^2\sigma_{12}|n|(n^2-1)}{12A_{12}R_1^3(\eta_2+\eta_1)}, \tag{16}$$

$$\Gamma(n) = -\frac{\dot{b}}{2b}|n| - \frac{b^2\sigma_{23}|n|(n^2-1)}{12A_{23}R_2^3(\eta_3+\eta_2)}, \tag{17}$$

$$\Omega(n) = -\frac{\dot{b}}{2b}|n| - \frac{b^2\sigma_{12}|n|(n^2-1)}{12A_{12}R_1^3(\eta_2+\eta_1)}, \tag{18}$$

$$\Xi(n) = -\frac{\dot{b}}{2b}\left(|n| + f_4^{-1}\right) - \frac{b^2\sigma_{23}|n|(n^2-1)}{12A_{23}R_2^3(\eta_3+\eta_2)}, \tag{19}$$

with $A_{12} = (\eta_2-\eta_1)/(\eta_2+\eta_1)$ [$A_{23} = (\eta_3-\eta_2)/(\eta_3+\eta_2)$] being the viscosity contrast between fluids 1 and 2 [2 and 3], and

$$f_1 = \frac{A_{12}(1 - A_{23}R^{2|n|})}{1 + A_{12}A_{23}R^{2|n|}}, \tag{20}$$

$$f_2 = \frac{A_{23}(1 + A_{12})R^{|n|-1}}{1 + A_{12}A_{23}R^{2|n|}}, \tag{21}$$

$$f_3 = \frac{A_{12}(1 - A_{23})R^{|n|+1}}{1 + A_{12}A_{23}R^{2|n|}}, \tag{22}$$

$$f_4 = \frac{A_{23}(1 + A_{12}R^{2|n|})}{1 + A_{12}A_{23}R^{2|n|}}. \tag{23}$$

The parameter R appearing in Eqs. (20)–(23) is defined as

$$R = \frac{R_1(t)}{R_2(t)} = \frac{R_1(0)}{R_2(0)} \tag{24}$$

and quantifies the coupling strength between the annular interfaces of the system [55–57], besides being related to the ring thickness. Therefore, it is evident that the two ordinary differential equations (ODEs) (14) and (15) are coupled through the terms proportional to f_2 and f_3 appearing on the right-hand side (r.h.s.) of these expressions, and that the coupling strength increases for larger values of R (with $0 < R < 1$). We also stress that as $R \to 0$, which corresponds to the physical situation where the two interfaces of the annulus are very far apart, $(f_2, f_3) \to 0$, and thus the interfaces decouple. In such a limit, there is no interaction between the interfaces, and their independent dynamics are described by Eqs. (14) and (15) with $f_1 \to A_{12}$, $(f_2, f_3) \to 0$, and $f_4 \to A_{23}$. In this specific scenario, Eqs. (14) and (15) reproduce the results from previous two-fluid, single interface lifting Hele-Shaw cell studies [11].

On the other hand, the opposite scenario, in which the interfaces are very close together and, therefore, strongly coupled, is achieved by taking the limit $R \to 1$. In this case, it is possible to show numerically [by using Eqs. (14) and (15)] that $\zeta_n \to \varepsilon_n$, and the interfacial dynamics corresponds to a single boundary between fluids 1 and 3 (without the presence of fluid 2), with surface tension equals to $\sigma_{12} + \sigma_{23}$.

The remaining nonlinear mode-coupling functions F, G, H, I, J, K, $\mathcal{F}$, $\mathcal{G}$, $\mathcal{H}$, $\mathcal{I}$, $\mathcal{J}$, and $\mathcal{K}$ appearing on the r.h.s. of Eqs. (14) and (15) are given in the Appendix [see Eqs. (A1)–(A20)].

It is known that weakly nonlinear analyses, as the one we employ in this paper, provide a more accurate description of the fluid-fluid interfacial dynamics in Hele-Shaw cell flows, when compared with conventional, purely linear stability studies (see, for instance, Refs. [4,45,55,56,58], and references therein). In fact, very important (and intrinsically nonlinear) morphological effects that emerge in Hele-Shaw flows, such as finger tip-sharpening, -broadening, and -splitting, as well as finger competition cannot be properly captured and described by linear stability analyses. A noteworthy advantage of weakly nonlinear analysis is that one is able to go up to longer times in the evolution of the system, while still respecting the validity of the perturbative method [i.e., $|\zeta| \ll R_1(t)$, and $|\epsilon| \ll R_2(t)$]. For these reasons, in this paper we carry out a second-order mode-coupling analysis of the lifting Hele-Shaw system with a fluid annulus, focusing on early nonlinear effects. Moreover, as we will see in Sec. IV, the contribution of viscous fingering to the adhesion force between the cell plates is of second order in the perturbation amplitudes [see Eq. (32)]. Therefore, also for the sake of consistency, throughout this paper, we present our results within the scope of a perturbative, second-order weakly nonlinear theory.

III. FINGERING STABILIZATION VIA A FLUID ANNULUS

In our perturbative, weakly nonlinear mode-coupling theory developed in Sec. II, the time evolution of the Fourier

amplitudes ζ_n and ε_n is key variables that dictate the evolution of the annular interfaces and the physical behaviors observed in the lifting-induced, three-fluid flow problem. Such quantities are obtained by numerically solving the nonlinear coupled ODEs (14) and (15) corresponding to each mode n. Then the inner and outer interfacial shapes are acquired through planar plots of the functions $\mathcal{R}_1(\theta,t) = R_1(t) + \zeta(\theta,t)$ and $\mathcal{R}_2(\theta,t) = R_2(t) + \varepsilon(\theta,t)$, with $0 \leqslant \theta \leqslant 2\pi$. However, note that ζ_n and ε_n appearing on the expressions corresponding to $\zeta(\theta,t)$ and $\varepsilon(\theta,t)$, i.e., Eqs. (1) and (2), respectively, are complex Fourier amplitudes. Therefore, to plot the interfaces one must first rewrite these complex amplitudes in terms of real-valued amplitudes. This is done by first defining $a_n(t) = \zeta_n(t) + \zeta_{-n}(t)$ and $b_n(t) = i[\zeta_n(t) - \zeta_{-n}(t)]$, which denote real-valued cosine and sine amplitudes for the inner boundary, respectively. Likewise, $\bar{a}_n(t) = \varepsilon_n(t) + \varepsilon_{-n}(t)$ and $\bar{b}_n(t) = i[\varepsilon_n(t) - \varepsilon_{-n}(t)]$ represent real-valued cosine and sine amplitudes for the outer interface. In terms of these new variables, we can express $\mathcal{R}_1(\theta,t)$ and $\mathcal{R}_2(\theta,t)$ as

$$\mathcal{R}_1(\theta,t) = R_1(t) + \zeta_0 + \sum_{n=1}^{N=40} [a_n(t)\cos(n\theta) + b_n(t)\sin(n\theta)] \tag{25}$$

and

$$\mathcal{R}_2(\theta,t) = R_2(t) + \varepsilon_0 + \sum_{n=1}^{N=40} [\bar{a}_n(t)\cos(n\theta) + \bar{b}_n(t)\sin(n\theta)]. \tag{26}$$

Note that in Eqs. (25) and (26), we have limited the number of participating modes to all n lying within the interval $1 \leqslant n \leqslant N = 40$. This upper limit ($N = 40$) for the number of participating modes is adopted for our weakly nonlinear analysis based on computational accuracy and cost considerations. More specifically, it was chosen after carrying out repeated and careful computations utilizing more participating modes ($40 < N \leqslant 70$), and our tests indicated that the interfacial patterns and perimeters obtained are almost indistinguishable from the results currently presented in this study for $N = 40$ (depicted in Figs. 2–5).

To maintain our theoretical analysis as close as possible to real-life lifting Hele-Shaw cell experimental conditions, we introduce background noise effects by assigning at $t = 0$ a random complex phase to each $\zeta_n(0)$ and $\varepsilon_n(0)$ mode amplitudes. The initial amplitude of each mode is given by $|\zeta_n(0)| = |\varepsilon_n(0)| = R_1(0)/2400$ and is independent of n. Moreover, as done in previous experimental [13–15] and theoretical [11,12,23] studies in lifting Hele-Shaw flows, all the analysis performed in this section considers that the upper plate moves with constant lifting speed $\dot{b} = v$ along the direction perpendicular to the cell plates, such that the gap width grows linearly with time as $b(t) = b_0 + vt$. Furthermore, we emphasize that the values we take for our parameters throughout the rest of this work are consistent with typical physical quantities used in experiments [13–15]. In these experimental studies, the viscosity of the central droplet can range from 10 to 500 Pa s, while v ranges from $O(10^{-7})$ m/s to $O(10^{-4})$ m/s. Typically, the surface tension is taken as 0.02 N/m, and the droplet's radius varies from 10^{-3} m to 2.0×10^{-2} m, while $10\,\mu\text{m} \leqslant b_0 \leqslant 800\,\mu\text{m}$.

Additionally, as pointed out in Sec. II, the description of the lifting Hele-Shaw flow in terms of Darcy's law requires that the cell gap width be always far smaller than a characteristic length scale in the plane of the cell, which one can take as the inner unperturbed radius, leading to the small-gap condition $b(t)/R_1(t) \ll 1$. In all the simulations presented in our work, $b(t_f)/R_1(t_f) = 0.045$ at the final time t_f, and, therefore, our results are within the small-gap condition. Also, note that such a condition can be rewritten explicitly in terms of the time t, yielding $t \ll t_{\text{crit}} = [(R_1(0)\sqrt{b_0})^{2/3} - b_0]/v$. This is useful if one wishes to estimate the maximum time beyond which Darcy's law description is not valid.

In most experiments concerning the traditional two-fluid, lifting Hele-Shaw flow, the usual configuration consists of a viscous fluid droplet surrounded by air, with a single fluid-fluid interface shrinking towards the center of the Hele-Shaw cell during the plate-lifting process. Inspired by such a conventional setting, in our current study, we also consider the outermost fluid as air, such that $\eta_3 \approx 0$. In addition, the innermost fluid is also taken as a very viscous oil of viscosity $\eta_1 = 200$ Pa s. However, in contrast to previous experimental [13–15] and theoretical [11,12,23] studies in lifting Hele-Shaw flows, here we introduce an additional finite fluid layer of viscosity η_2 separating the inner and outermost regions. Therefore, in this section, our primary goal is to analyze how this new fluid annulus impacts the morphology and stability of the interface of the central oil droplet. To explore these aspects, two very important governing parameters are varied, namely, the annulus viscosity η_2 and the annulus thickness (related to the coupling parameter R). Under these considerations, we initiate our morphological and stability analysis by examining Fig. 2, which displays snapshots taken at time $t = 300$ s of representative weakly nonlinear patterns formed during three-fluid, lifting Hele-Shaw flow. We stress that this final time value ($t = 300$ s) is consistent with the typical times associated with early nonlinear stages of the dynamics presented in Refs. [13–15].

For a given row in Fig. 2, the three displayed patterns are plotted considering increasingly larger values for the intermediate fluid viscosity η_2, so that $\eta_2 = 10$ Pa s for (a), (d), and (g), $\eta_2 = 30$ Pa s for (b), (e), and (h), and $\eta_2 = 50$ Pa s for (c), (f), and (i). Furthermore, the coupling parameter R varies through each row, being equal to $R = 0.6$, $R = 0.75$, and $R = 0.9$ for the first, second, and third rows, respectively. Such variation on R corresponds to a decrease in the annulus thickness from the top to bottom in Fig. 2. The remaining physical parameters are set as $R_1(0) = 0.01$ m, $b_0 = 200\,\mu$m, $v = 5 \times 10^{-7}$ m/s, and $\sigma_{12} = \sigma_{23} = 0.02$ N/m. We stress that, although we illustrate our results by using this particular set of representative parameter values, we have tested several others and found behaviors similar to those we report here. This fact supports the generality of our representative findings.

We initiate our discussion by examining the pattern portrayed in Fig. 2(a), formed under a low value of η_2 and a relatively thick annulus. It is evident that while the inner

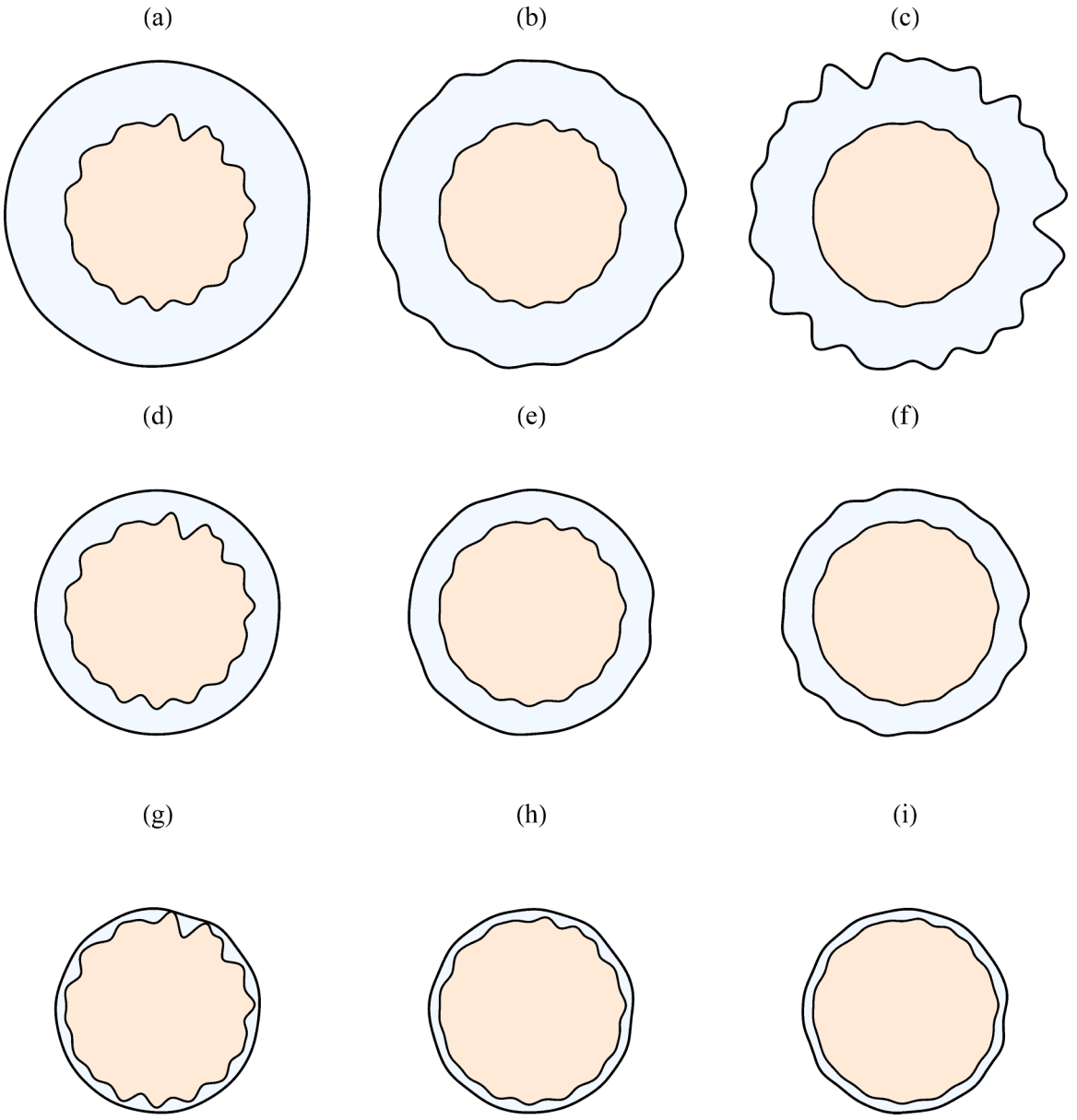

FIG. 2. Snapshots of representative weakly nonlinear interfacial patterns formed during the lifting Hele-Shaw flow of three fluids for $R = 0.6$ (a–c), $R = 0.75$ (d–f), and $R = 0.9$ (g–i). In each row, the annulus viscosity increases from left to right, assuming the values $\eta_2 = 10$ Pa s (a, d, g), $\eta_2 = 30$ Pa s (b, e, h), and $\eta_2 = 50$ Pa s (c, f, i). All the snapshots are taken at $t = 300$ s, and the patterns are plotted considering the coupling of all sine and cosine Fourier modes lying within the interval $1 \leqslant n \leqslant 40$, with random initial phases for each participating mode. In addition, consistent with existing two-fluid, single interface experiments in lifting Hele-Shaw cells [13–15], we set $\eta_1 = 200$ Pa s, $\eta_3 = 0$, $R_1(0) = 1$ cm, $b_0 = 0.2$ mm, $v = 5 \times 10^{-7}$ m/s, and $\sigma_{12} = \sigma_{23} = 0.02$ N/m.

interface deforms, presenting multiple fingering undulations, the outer boundary of the fluid ring remains essentially a circle, despite the existence of a positive viscosity jump between the outermost fluid and the intermediate annular region. As the intermediate fluid viscosity increases to $\eta_2 = 30$ Pa s while all the other physical parameters remain unchanged, one observes that such a variation affects the generated pattern shown in Fig. 2(b) by turning the inner (outer) interface less (more) perturbed when compared with the three-fluid structure depicted in Fig. 2(a). Further increasing η_2 to 50 Pa s, as presented in Fig. 2(c), we see that the effects already pointed out in Fig. 2(b) become more prominent: while the inner boundary is now mildly perturbed, the external interface of the ring presents very sizable, well-developed, viscous fingers. The observed stability and instability effects found in the analysis of Figs. 2(a)–2(c) as η_2 varies have a simple explanation: by increasing η_2, one simultaneously enhances the viscosity difference between fluids 2 and 3 while diminishing this quantity for fluids 1 and 2. Thus, the annulus outer and inner boundaries become increasingly unstable and stable, respectively.

The results obtained from Figs. 2(a)–2(c) indicate that an air-oil interface (as the one that normally appears in common two-fluid, single interface lifting Hele-Shaw flows, and fluid adhesion problems [13–15,20–23]) can be stabilized by enveloping the central oil droplet with a thick fluid ring of

intermediate viscosity between the air and oil viscosities. Nevertheless, such an application of the fluid annulus on the inner interface stabilization appears to be of limited use since very pronounced fingers emerge on the outer interface due to the strong Saffman-Taylor instability between fluids 2 and 3 [see Fig. 2(c)]. Eventually, this intense interface destabilization between fluids 2 and 3 would induce the rupture of the fluid annulus, as one of these protuberances reach the inner boundary. Unfortunately, this rupture would break the integrity of the fluid ring, and cease the stabilization effects induced by the annulus. However, it is worth recalling that besides η_2, our system also allows variations on the annulus thickness by increasing the value of the coupling parameter R.

To probe into additional stabilization possibilities by using a thinner annulus, we turn our attention to the analysis of the second row of Fig. 2 [Figs. 2(d)–2(f)], which depicts three-fluid patterns for $R = 0.75$, and the same viscosities utilized in Figs. 2(a)–2(c). An initial inspection of the inner interfaces of the annular structures presented in the three-fluid patterns of Figs. 2(d)–2(f) does not reveal a significantly different scenario from the one already seen in Figs. 2(a)–2(c). That is, as η_2 increases from left to right, the inner interface becomes more and more stable. One can also verify that the inner interfaces in Figs. 2(d)–2(f) for $R = 0.75$ are very similar to those illustrated in Figs. 2(a)–2(c) for $R = 0.6$. This indicates that the inner interface stabilization effect produced by the annulus is independent of its thickness.

On the other hand, by comparing Figs. 2(a)–2(c) with Figs. 2(d)–2(f) it is also noticeable that the annulus thickness strongly impacts the stability and morphology of the outer interface of the fluid ring. Even when a large value of η_2 is considered, as in Fig. 2(f), the outer boundary of the annulus is just moderately disturbed. Such a slightly undulated outer interface differs considerably from the very perturbed fingered structure shown in Fig. 2(c) for $R = 0.6$. As in other circumstances involving fluid rings in Hele-Shaw flows [55–57], this physical behavior is caused by the augmented coupling between inner and outer annular interfaces for smaller thicknesses. Since we have increased the coupling parameter from $R = 0.6$ (first row of Fig. 2) to $R = 0.75$ (second row of Fig. 2), the stability of each interface becomes more dependent on the coupling between them, and less determined by the viscosity difference between fluids 2 and 3, as it used to be in usual one-interface, two-fluid Hele-Shaw flows. Therefore, the combination of a thin annulus with a large viscosity η_2 has led to a nearly stable central droplet surrounded by a slightly undulated fluid ring, highlighting the usefulness of the fluid annulus strategy in controlling the emergence of Saffman-Taylor instabilities on the interface of the central shrinking droplet in lifting flows.

We close our discussion of Fig. 2 by considering the influence of an even thinner fluid ring ($R = 0.9$), as depicted in Figs. 2(g)–2(i). Notice that all the effects already mentioned in the previous analysis of Figs. 2(a)–2(f) are enhanced. While the inner interface stabilization is mainly controlled by the fluid ring viscosity η_2, its thickness is responsible for maintaining the outer boundary stability. It is worthwhile to note that the utilization of a very thin fluid annulus in Fig. 2(i) is perfectly capable of inducing an efficient stabilization of the central droplet interface, while maintaining the structural integrity of the fluid ring by avoiding its rupture. Thus, the weakly nonlinear results obtained from Fig. 2 suggest that if one seeks to minimize the emergence of instabilities on an oil droplet boundary surrounded by air during lifting Hele-Shaw flows, then enveloping it with a thin, viscous fluid ring is indeed a suitable and effective strategy.

In Fig. 2 we have found a number of useful results concerning morphological aspects of the fluid ring inner and outer boundaries, as well as the possibility of using the intermediate annulus to stabilize the central oil droplet interface during the plate-lifting process. Such conclusions were obtained by visual comparison of the generated three-fluid patterns. In Fig. 3 we complement the previous visually-based analysis by providing more quantitative data, namely, the time evolution of the rescaled interfacial perimeters of the intermediate fluid annulus, defined as

$$L_i(t) = \frac{1}{2\pi R_i(t)} \int_0^{2\pi} \sqrt{\mathcal{R}_i^2(\theta,t) + \left[\frac{d\mathcal{R}_i(\theta,t)}{d\theta}\right]^2}\, d\theta, \quad (27)$$

associated with the structures displayed in Fig. 2. In Eq. (27), the subscript $i = 1$ ($i = 2$) refers to the rescaled perimeter of the inner (outer) interface of the fluid ring. In addition, $L_i(t)$ measures how much the perturbed fluid-fluid interface perimeter deviates from the corresponding unperturbed perimeter $2\pi R_i(t)$. Each column of Fig. 3 is associated with a row of Fig. 2. In this way the time evolution of the perimeters $L_1(t)$ and $L_2(t)$ portrayed respectively in Figs. 3(a) and 3(d) for $0 \leqslant t \leqslant 300$ s are related to the inner and outer interfaces of the three-fluid patterns illustrated in Figs. 2(a)–2(c) for $t_f = 300$ s and $R = 0.6$. Likewise, the data shown in Figs. 3(b) and 3(e) [Figs. 3(c) and 3(f)] correspond to situations pictured in Figs. 2(d)–2(f) for $R = 0.75$ [Figs. 2(g)–2(i) for $R = 0.9$].

In Fig. 3(a) the dotted curves correspond to the time evolution of $L_1(t)$ considering the same three values of η_2 that have been used in Fig. 2. Since we intend to demonstrate the fluid annulus capability of stabilizing the inner interface perimeter, we have also added a solid curve labeled as "Single interface" representing the evolution of $L_1(t)$ without the intermediate fluid envelope, i.e., the case in which air (fluid 3) displaces the central oil droplet (fluid 1) directly, without the presence of an annulus (fluid 2). It is quite evident that the fluid annulus exerts a significant effect on the inner interface stability. For $t > 0$, one observes that all the dotted curves lie below the solid one and verifies that the stabilization effect caused by the fluid ring is stronger for larger viscosity values η_2. On the other hand, the "Single interface" perimeter keeps growing as time progresses. Thinner fluid envelopes are considered in Figs. 3(b) and 3(c). Nevertheless, the two graphs portrayed in these figures look exactly like the one already shown in Fig. 3(a). These facts quantitatively reinforce what we have found in Fig. 2 about the inner interface stabilization effect induced by the annulus being independent of its thickness, and dictated mainly by its viscosity η_2.

The graphs on the bottom of Fig. 3 show how variations in η_2 and R affect the time evolution of $L_2(t)$. By inspecting Fig. 3(d), we see that larger values of η_2 increase the outer interface perimeter, enhancing interfacial instabilities on the annulus external boundary. As the annulus thickness is reduced, as in Fig. 3(e) for $R = 0.75$ and 3(f) for $R = 0.9$,

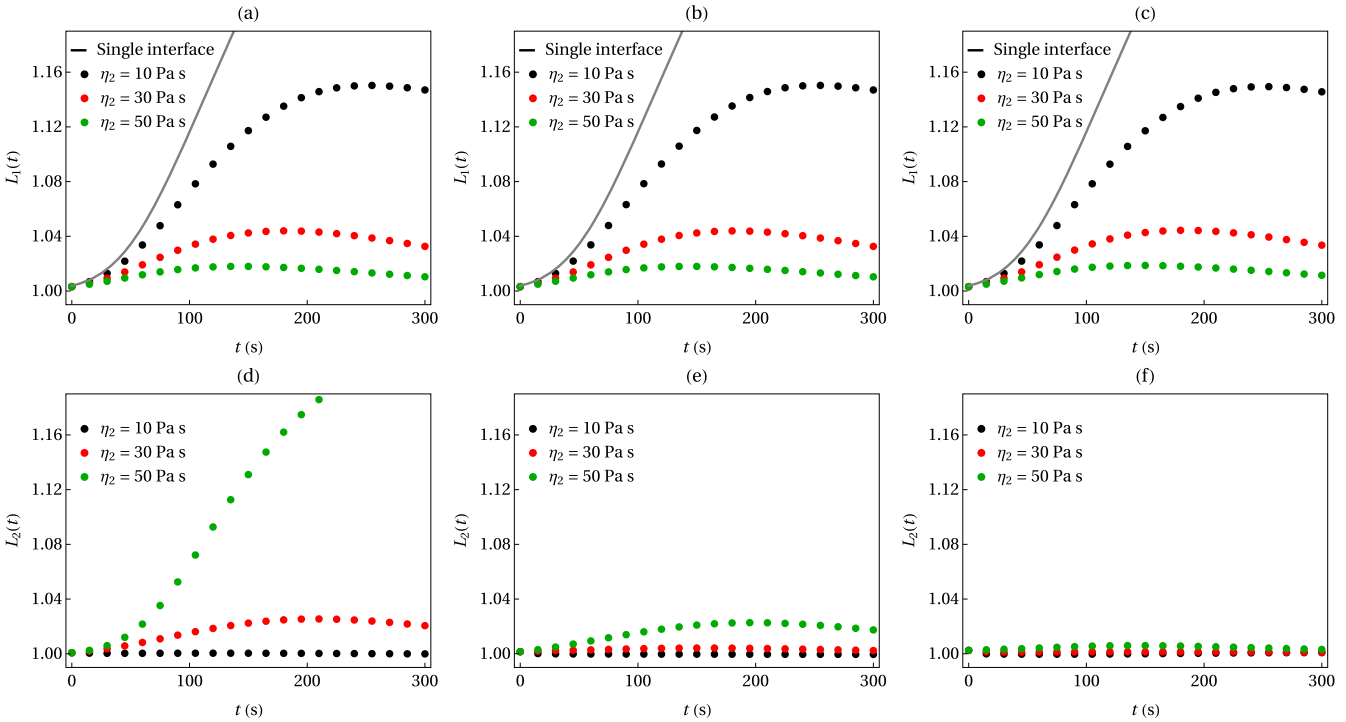

FIG. 3. Time evolution of the inner (a–c) and outer (d–f) interfacial perimeters $L_1(t)$ and $L_2(t)$ of the intermediate fluid annulus, respectively, for the situations depicted in Fig. 2. The perimeters' evolutions portrayed in (a) and (d) for $0 \leqslant t \leqslant 300$ s are related to the patterns snapshots illustrated in Figs. 2(a)–2(c) for $t = 300$ s. Likewise, the data shown in (b) and (e) (c and f) correspond to situations pictured in Figs. 2(d)–2(f) [Figs. 2(g)–2(i)]. All the physical parameters used here are identical to those utilized in Fig. 2. Note that in (a)–(c) we have included solid curves (labeled as "Single interface") associated with the evolutions of $L_1(t)$ in the traditional lifting Hele-Shaw flow setup in which only two fluids separated by a single interface are involved (i.e., the case in which fluid 3 displaces fluid 1 directly, without the presence of an annulus of fluid 2).

all the $L_2(t)$ curves tend to approach the horizontal axis, and are not significantly influenced by the η_2 values as in the case depicted in Fig. 3(d) for a thicker annulus. These findings once again support one of the main results extracted from Fig. 2: thinner fluid annuli have less perturbed outer boundaries than thicker ones, and thus are more appropriate to be used as an instability control tool in lifting Hele-Shaw cell flows.

During the analysis of Figs. 2 and 3, our findings pointed out to the annulus viscosity η_2 as a key parameter regulating the inner interface stabilization. However, there is also another potential contributing factor coming from surface tension effects through coupling mechanisms. Recall that in the limit of a very thin fluid annulus, $R \to 1$. Under this circumstance, Eqs. (14) and (15) reduce exactly to the same expression, both describing the dynamics of an interface positioned between the outer fluid 3 and the central droplet of fluid 1, with surface tension equal to $\sigma_{12} + \sigma_{23}$. Therefore, this important limit informs us that as R gets closer to unit, as in the case of $R = 0.9$ utilized in Figs. 2 and 3, the surface tension σ_{23} coming from the outer interface of the annulus could as well contribute to the inner interface stabilization.

To investigate which parameter contributes the most to the inner interface stabilization effect, in Fig. 4 we plot the time evolution of the inner interfacial perimeter $L_1(t)$ for a thin annulus having $R = 0.9$, and three different sets of outer interface surface tension σ_{23}, and annulus viscosity η_2: (i) $\sigma_{23} = 0.02$ N/m and $\eta_2 = 10$ Pa s, (ii) $\sigma_{23} = 0.1$ N/m and $\eta_2 = 10$ Pa s, and (iii) $\sigma_{23} = 0.02$ N/m and $\eta_2 = 50$ Pa s. The remaining physical parameters are the same as in Fig. 2.

The parameter sets (i) and (ii) differ only by the σ_{23} values, which are five times larger in set (ii) than in (i). By comparing the dotted curves associated with these two parameter sets, we note that the larger σ_{23} value related to set (ii) only slightly reduces the perimeter $L_1(t)$ in comparison to the perimeter plotted for set (i). On the other hand, parameter set (iii) has the same σ_{23} value of set (i) and considers a viscosity η_2 five times larger than the viscosities of (i) and (ii). The impact of such a large value of η_2 on the time evolution of $L_1(t)$ is apparent since the dotted curve associated with (iii) is far below the two dotted curves related to (i) and (ii). The results indicate that although a thinner annulus leads to an increased coupling between the two interfaces of our system, the observed inner interface stabilization is mainly determined by viscosity effects rather than by surface tension.

IV. ADHESION FORCE: INFLUENCE OF A FLUID ANNULUS

In Sec. III we investigated pattern formation aspects arising during three-fluid, lifting Hele-Shaw flows, focusing on morphological and stability behaviors of the outer and inner boundaries of the intermediate annulus. Nevertheless, as commented earlier in this paper, the lifting flow of confined viscous fluids is also connected to another important physical aspect: namely, the bond strength of stretched

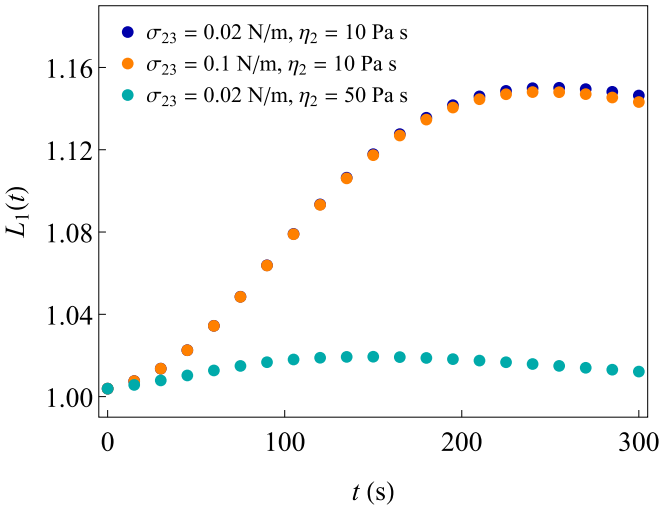

FIG. 4. Time evolution of the inner interfacial perimeter $L_1(t)$ of the intermediate fluid annulus for $R = 0.9$, and three different sets of outer interface surface tension σ_{23}, and annulus viscosity η_2: (i) $\sigma_{23} = 0.02$ N/m and $\eta_2 = 10$ Pa s, (ii) $\sigma_{23} = 0.1$ N/m and $\eta_2 = 10$ Pa s, and (iii) $\sigma_{23} = 0.02$ N/m and $\eta_2 = 50$ Pa s. The rest of the physical parameters are equal to the ones used in Fig. 2.

liquids sandwiched between solid plates, something measured via probe-tack adhesion tests [17–19]. Therefore, in this section our goal is to quantify the effects of the intermediate fluid annulus on the adhesion force, during the three-fluid-stretching process. To do it, we use the lifting Hele-Shaw cell flow results derived in Sec. II, and calculate the pulling force $F = F(t)$ required to detach the parallel flat plates "glued" together by such an annular fluid system. Then we examine how the viscosity of the fluid ring η_2 and the thickness of the annulus (related to the parameter R) affect the adhesion force. We also compare the behavior of the pulling force in the presence of the fluid annulus, with the corresponding response obtained when fluid envelope contributions are neglected.

As described in Sec. III, we consider that the upper plate is lifted at a given speed, so that the external pulling force $\mathbf{F} = F\mathbf{e_z}$ should balance the fluid pressure force $\mathbf{F}_p = F_p\mathbf{e_z}$, where $\mathbf{e_z}$ is the upward unit vector perpendicular to the plates. In this framework, F can be calculated by integrating the pressure field p over the areas Ω_1 and Ω_2 occupied, respectively, by viscous fluids 1 and 2, i.e.,

$$F = -F_p = -\int_{\Omega_1,\Omega_2} p dA. \tag{28}$$

Note that the outermost fluid 3 does not contribute to F since its viscosity $\eta_3 \approx 0$. Hence, pressure p_3 is constant, and we set it to zero without loss of generality. On the other hand, the pressure fields within fluids 1 and 2 are obtained by first rewriting the gap-averaged velocity $\mathbf{v}_j$ in terms of the velocity potential ϕ_j and then substituting them in the left-hand side (l.h.s.) of Eq. (5), leading to the relations $p_j = 12\eta_j\phi_j/b^2$, where $j = 1, 2$, and 3. Next, we consider Eqs. (11)–(13) to express the pressure fields as

$$p(r,\theta) = \begin{cases} p_1(r,\theta) & \text{if } r < \mathcal{R}_1, \\ p_2(r,\theta) & \text{if } \mathcal{R}_1 < r < \mathcal{R}_2, \\ 0 & \text{if } \mathcal{R}_2 < r, \end{cases} \tag{29}$$

where

$$p_1(r,\theta) = \frac{3\eta_1\dot{b}r^2}{b^3} + \frac{12\eta_1}{b^2}\sum_n \alpha_n(t)\left(\frac{r}{R_1}\right)^{|n|} e^{in\theta} \tag{30}$$

and

$$p_2(r,\theta) = \frac{3\eta_2\dot{b}r^2}{b^3} + \frac{12\eta_2}{b^2}\sum_n \beta_n(t)\left(\frac{r}{R_1}\right)^{-|n|} e^{in\theta} + \frac{12\eta_2}{b^2}\sum_n \gamma_n(t)\left(\frac{r}{R_2}\right)^{|n|} e^{in\theta}. \tag{31}$$

Finally, the force required to lift the upper plate is obtained after solving Eq. (28) considering the pressure fields (29), yielding

$$\begin{aligned} F = {} & \frac{3\pi\dot{b}}{2b^3}\left[\eta_1 R_1^4 + \eta_2\left(R_2^4 - R_1^4\right)\right] \\ & + \sum_{n\neq 0}\left\{\frac{3\dot{b}\pi}{b^3}\left[R_1^2(\eta_1-\eta_2)|\zeta_n|^2 + R_2^2\eta_2|\varepsilon_n|^2\right]\right. \\ & - \frac{12\pi}{b^2}\left[f_2 R_1^2\Gamma(n)\varepsilon_n\zeta_{-n} + f_1 R_1^2(\eta_1-\eta_2)\Lambda(n)|\zeta_n|^2\right. \\ & \left.\left. + R_2^2\eta_2(f_4\Xi(n)|\varepsilon_n|^2 + f_3\Omega(n)\zeta_n\varepsilon_{-n})\right]\right\}. \end{aligned} \tag{32}$$

Equation (32) is a central result of this section, accounting for the influence of the fluid annulus of viscosity η_2 enveloping the central viscous droplet of viscosity η_1 on the adhesion force. Note that the time dependence of F in Eq. (32) is implicit in $b = b(t)$. In addition, the summation appearing in the second line of Eq. (32) represents the contribution up to second order in the perturbations amplitudes ζ_n and ε_n coming from the fingering formation on the annulus boundaries. Recall that the functions f_1, f_2, f_3, and f_4 appearing in Eq. (32) are given in Eqs. (20)–(23). Likewise, the functions $\Lambda(n)$, $\Gamma(n)$, $\Omega(n)$, and $\Xi(n)$ present in Eq. (32) are expressed by Eqs. (16)–(19). It should be pointed out that, consistent with experimental findings, we have verified that for the strongly confined, very viscous fluids used here, and in Refs. [14,20,23,24,59,60], surface tension contributions [see Eqs. (7) and (9)] to the adhesion force (32) are very small and can be neglected. However, surface tension effects are still relevant for calculating the interfacial perturbation amplitudes ζ_n and ε_n. We call the reader's attention that if one seeks to evaluate the adhesion force in the single interface limit, the integration in Eq. (28) must be performed over the area occupied by the central droplet of fluid 1, i.e., from $r = 0$ to $r = \mathcal{R}_1$ in polar coordinates.

In real probe-tack adhesion tests, the experimental apparatus utilized for lifting the upper Hele-Shaw cell plate is not rigid and deforms as the plate-lifting process occurs. The compliance of the measurement apparatus is responsible for

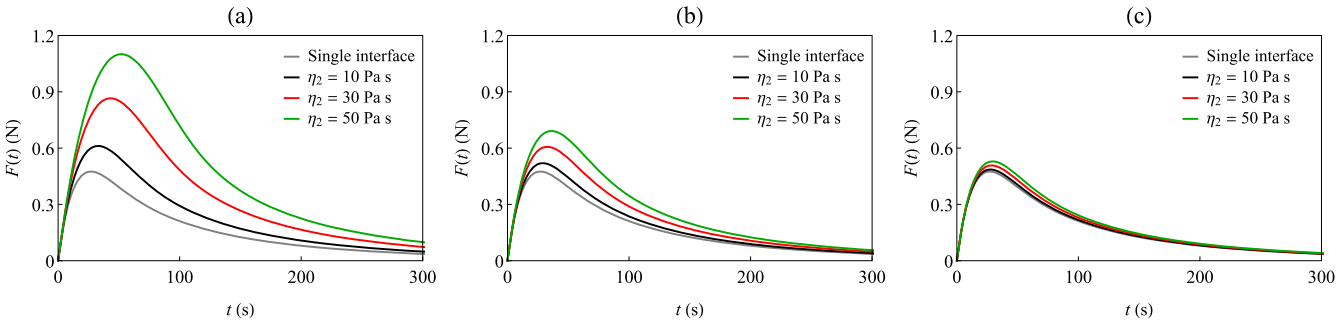

FIG. 5. Adhesion force $F(t)$ as a function of time t for (a) $R = 0.6$, (b) $R = 0.75$, and (c) $R = 0.9$. Here the viscosity of the annular layer η_2 is taken as 10, 30, and 50 Pa s. All the other physical parameters are the same as in Fig. 2. As in Fig. 3, here we have also added solid curves corresponding to the lifting force obtained in the usual fluid adhesion arrangement involving only two fluids (e.g., a viscous oil and air) and a single interface.

the typical adhesion force curve shape evaluated in probe-tack tests, which usually starts with a sharp increase of the force once the probe is pulled apart. Then the force quickly reaches its maximum and drops asymptotically to zero as the plate-plate separation is increased (see, for example, Figs. 1 and 2 of Ref. [59], or Fig. 5 in this paper). To implement the compliance effect in our theoretical analysis, we follow Refs. [19,20,24,59,60] and assume that the apparatus has a spring constant denoted by k. At a given time t, the plate spacing is $b = b(t)$, while the deformation due to the stretching of the apparatus is $L(t) - b(t)$, where at $t = 0$ we have $b(0) = L(0)$. We direct the readers to Refs. [24,60] for illustrative sketches of the probe-tack apparatus with the definition of the geometrical quantities b and L. Note that due to the compliance of the measurement apparatus, the actual plate spacing b is not necessarily equivalent to L, except for the case of a completely rigid configuration. Therefore, the presence of the compliance yields an interplay between the viscous force $F = F(b, \dot{b})$, quantified by Eq. (32), and a spring restoring force $k(L - b)$, which results from the deflection of the apparatus, determined by the nonlinear differential equation [19,20,59]

$$k(L - b) = F(b, \dot{b}), \tag{33}$$

obtained after neglecting the apparatus inertia.

In existing probe-tack instruments, the control parameter set by the flexible apparatus's motors is L, not b. Consistent with these real experimental setups and theoretical works on fluid adhesion phenomena, we consider that L evolves in time according to the expression $L(t) = b_0 + vt$. So, in order to obtain the temporal evolution of b, one first has to substitute Eq. (32) into Eq. (33). Then the resulting ODE is solved numerically for $b(t)$. This numerical outcome is plugged back into Eq. (32), and thus, we finally obtain the force F as a function of time t.

In order to understand the consequences of wrapping a central oil droplet with a viscous fluid annulus in the adhesion phenomenon, in Fig. 5 we plot the adhesion force $F(t)$ against the time t for different annulus thicknesses, so that we have in (a) $R = 0.6$, (b) $R = 0.75$, and (c) $R = 0.9$. In addition, we also consider the same three values for the annulus viscosity that has been used in Figs. 2 and 3, i.e., $\eta_2 = 10$, 30, and 50 Pa s. Consistent with probe-tack instruments, we set $k = 10^5$ N/m [19,20,24,59,60], and the remaining physical parameters are the same as in Fig. 2.

Figure 5(a) illustrates the case associated with a thick fluid annulus, as quantified by the parameter $R = 0.6$. First, we note that the typical adhesion curve shape is preserved even when considering the fluid envelope's presence, as well as the fingering formation on the annulus boundaries. However, by comparing the three curves for the different viscosities related to the fluid annulus with the one associated with the single interface case, it is clear that the presence of the annulus not only increases the adhesion force peak (adhesion strength), but also delays the rate at which the force decays asymptotically to zero. Such effects are significantly augmented as η_2 is increased. Therefore, the addition of a thick fluid ring surrounding a central oil droplet modifies the adhesion properties by increasing the force required to detach the parallel plates of the lifting apparatus.

Nevertheless, for thinner fluid annuli, as the ones considered in Fig. 5(b) for $R = 0.75$, and Fig. 5(c) for $R = 0.9$, fluid annulus effects on the adhesion force become less and less pronounced. In Fig. 5(b) the difference between the four curves is still noticeable although less evident than the situation depicted in Fig. 5(a) for a thicker fluid ring. On the other hand, the difference between the curves in Fig. 5(c) is barely noticeable, with all the annulus cases approaching the single interface situation regardless of the viscosity η_2. This can be understood by recalling that the adhesion force [Eqs. (28)–(32)] is proportional to the area of the viscous fluids in contact with the upper plate of the lifting apparatus. We increase $R = R_1(0)/R_2(0)$ by keeping $R_1(0)$ fixed, while decreasing the value of $R_2(0)$. This is equivalent to maintaining the contact area of fluid 1 with the upper plate constant, and reducing the corresponding contact area of fluid 2, leading to a decrease in the adhesion force. This latter result, together with the findings presented in Figs. 2 and 3, demonstrates the possibility of utilizing fluid envelopes to stabilize an oil droplet interface during lifting plate flows without modifying the adhesion force significantly, as long as the fluid envelope is sufficiently thin.

As a last remark of this section, we point out that we have also analyzed the adhesion force without considering the fingering formation. Such a scenario is achieved by setting ζ_n and ε_n to zero in Eq. (32). Within our perturbative, second-order, weakly nonlinear theory, and for the physical parameters considered in this work, our results indicate that the fingering instability arising on the boundaries of the fluid annulus has

a very modest effect on the adhesion curve, even for the case with $R = 0.6$, where considerably developed fingers are present on the interfaces [see the patterns in Figs. 2(a)–2(c)]. These findings are in line with the experimental results reported in Ref. [54] regarding the adhesion strength being almost independent of the Saffman-Taylor instabilities.

V. CONCLUSION

In recent years there has been increased interest in studying how to control, and eventually suppress, the development of the viscous fingering instability in the confined environment of Hele-Shaw cells. In particular, much attention has been devoted to manipulating such instabilities for injection-driven flows in Hele-Shaw cells with fixed gap width (see, for instance, Refs. [34–51], and references therein). Curiously, equivalent explorations in variable-gap Hele-Shaw cells have received comparatively much less attention in the literature. Only very recently, some research groups started to devise strategies to control or minimize the emergence of fingering instabilities in the time-dependent gap, lifting Hele-Shaw flows [52–54].

In the light of the disparity in the amount of research done on the control of the Saffman-Taylor instability in Hele-Shaw cells with fixed and variable gap widths, and encouraged by the stimulating results reported in Refs. [52–54], in this paper we propose an alternative control method seeking to suppress viscous fingering formation in lifting Hele-Shaw flows. Our control scheme is realized by taking advantage of the presence of a viscous fluid annulus, separating a central fluid droplet of larger viscosity, from an infinite fluid domain of negligible viscosity.

By employing a mode-coupling perturbative approach to describe the time evolution of the annulus inner and outer boundaries at the onset of nonlinearities, we have found that depending on the value of the fluid ring viscosity, and on the thickness of such annular layer, one can restrain interfacial instabilities. More specifically, we have shown that while the stability behavior of the inner interface of the annulus is largely regulated by the viscosity of the fluid ring, the annulus thickness has control over the stability of the outer boundary. Our results indicate that increased interface stabilization is achieved by using thinner annuli of relatively large viscosities. These findings support the idea that the utilization of such a viscous thin annulus constitutes a very simple and effective stabilization strategy for lifting Hele-Shaw cell flows.

We have also investigated how the ring's viscosity and thickness, as well as the presence of fingering at the inner and outer boundaries of the ring, affect the adhesion force between the plates. We found that for a given annulus thickness, fluid rings having larger viscosities lead to augmented adhesive strengths. On the other hand, for a given value of the fluid ring viscosity, increasingly thinner annuli result in lower adhesive strengths. Furthermore, we have verified that the adhesion forces for thinner annuli of different viscosities are nearly identical, indicating that the use of thinner fluid rings to stabilize fingering instabilities can be done without changing the adhesion force substantially. Finally, we have detected no distinction in the adhesion force computed for stable or unstable annular interfaces, indicating that the presence of fingering at the ring's boundaries has an inconsequential effect on the adhesion force.

We conclude by briefly outlining some possible extensions of this work. These extensions may include the utilization of annular rings composed of non-Newtonian fluids (e.g., shear-thinning and shear-thickening fluids [61,62]), or keep the intermediate annulus as a Newtonian fluid, but considering the inner and outer boundaries of it as elastic interfaces [63–65]. Another interesting possibility is to consider a Newtonian fluid ring bounded by inner and outer interfaces that possess nontrivial interfacial rheology properties [58,66,67]. In addition, one could examine the intermediate fluid annulus as being a magnetic fluid (ferrofluid [68] or magnetorheological fluid [69,70]), and use an externally applied magnetic field to try to control interfacial instabilities and fluid adhesion in lifting Hele-Shaw cell flows. Moreover, one could still explore an electro-osmotic flow [49–51] of the annulus under the influence of an applied electric field during the lifting process.

ACKNOWLEDGMENTS

J.A.M. thanks CNPq (Conselho Nacional de Desenvolvimento Científico e Tecnológico) for financial support under Grant No. 305140/2019-1. I.M.C. wishes to thank CNPq (Conselho Nacional de Desenvolvimento Científico e Tecnológico) for financial support through Grant No. 140175/2022-9. R.M.O. and P.H.A.A. acknowledge support from the Brazilian National Agency for Petroleum, Natural Gas and Biofuels through the Human Resources Program, PRH-ANP, under Grant No. 01.19.0248.00, Ref. No. 0420/19. R.M.O also thanks CNPq for financial support through Grant No. 409195/2023-5.

APPENDIX : SECOND-ORDER MODE-COUPLING FUNCTIONS

In this Appendix we give the expressions for the second-order mode-coupling functions which have been presented in Sec. II. The second-order functions appearing in Eq. (14) are written as

$$F(n,p) = \frac{|n|}{R_1}\left\{\frac{\dot{b}}{2b}\left[\frac{1}{2} - g_1(n,p)\mathrm{sgn}(np) - \frac{f_1^{-1}}{|n|}\right] - \frac{b^2\sigma_{12}}{12A_{12}R_1^3(\eta_2+\eta_1)}\left[1-(3p+n)\frac{p}{2}\right]\right\}, \tag{A1}$$

$$G(n,p) = \frac{1}{R_1}\left\{|n|[1-g_1(n,p)\mathrm{sgn}(np)] - f_1^{-1}\right\}, \tag{A2}$$

$$H(n,p) = \frac{|n|}{R_2}\left\{\frac{\dot{b}}{2b}\left[\frac{1}{2} - g_2(p)\mathrm{sgn}(np)\right] - \frac{b^2\sigma_{23}}{12A_{23}R_2^3(\eta_3+\eta_2)}\left[1-(3p+n)\frac{p}{2}\right]\right\}, \tag{A3}$$

$$I(n,p) = \frac{|n|}{R_2}\{1 - g_2(p)\mathrm{sgn}(np)\}, \tag{A4}$$

$$J(n,p) = \frac{|n|}{R_1}\frac{\dot{b}}{2b}\left(\frac{R^{|p|-|n|}(1+A_{23}R^{|n|})}{A_{23}(1-R^{2|p|})}\right)\mathrm{sgn}(np), \tag{A5}$$

$$K(n,p) = \frac{|n|}{R_1}\left(\frac{R^{|p|-|n|}(1+A_{23}R^{|n|})}{A_{23}(1-R^{2|p|})}\right)\mathrm{sgn}(np), \tag{A6}$$

$$L(n,p) = \frac{|n|}{R_1}\frac{\dot{b}}{2b}\left(\frac{(1+A_{23})R^{2+|p|}}{A_{23}(1-R^{2|p|})}\right)\mathrm{sgn}(np), \tag{A7}$$

$$M(n,p) = \frac{|n|}{R_1}\left(\frac{(1+A_{23})R^{2+|p|}}{A_{23}(1-R^{2|p|})}\right)\mathrm{sgn}(np), \tag{A8}$$

where

$$g_1(n,p) = \frac{A_{12}+A_{23}R^{2|n|}+R^{2|p|}+A_{12}A_{23}R^{2(|n|+|p|)}}{A_{12}(1-A_{23}R^{2|n|})(1-R^{2|p|})} \tag{A9}$$

and

$$g_2(p) = \frac{1+A_{23}}{A_{23}(1-R^{2|p|})}. \tag{A10}$$

The second-order expressions in Eq. (15) are given by

$$\mathcal{F}(n,p) = \frac{|n|}{R_1}\left\{\frac{\dot{b}}{2b}\left[\frac{1}{2} - g_3(p)\mathrm{sgn}(np)\right] - \frac{b^2\sigma_{12}}{12A_{12}R_1^3(\eta_2+\eta_1)}\left[1-(3p+n)\frac{p}{2}\right]\right\}, \tag{A11}$$

$$\mathcal{G}(n,p) = \frac{|n|}{R_1}[1 - g_3(p)\mathrm{sgn}(np)], \tag{A12}$$

$$\mathcal{H}(n,p) = \frac{|n|}{R_2}\left\{\frac{\dot{b}}{2b}\left[\frac{1}{2} - g_4(n,p)\mathrm{sgn}(np) - \frac{f_4^{-1}}{|n|}\right] - \frac{b^2\sigma_{23}}{12A_{23}R_2^3(\eta_3+\eta_2)}\left[1-(3p+n)\frac{p}{2}\right]\right\}, \tag{A13}$$

$$\mathcal{I}(n,p) = \frac{1}{R_2}\left\{|n|[1 - g_4(n,p)\mathrm{sgn}(np)] - f_4^{-1}\right\}, \tag{A14}$$

$$\mathcal{J}(n,p) = \frac{|n|}{R_2}\frac{\dot{b}}{2b}\left(\frac{(A_{12}-1)R^{|p|-2}}{A_{12}(1-R^{2|p|})}\right)\mathrm{sgn}(np), \tag{A15}$$

$$\mathcal{K}(n,p) = \frac{|n|}{R_2}\left(\frac{(A_{12}-1)R^{|p|-2}}{A_{12}(1-R^{2|p|})}\right)\mathrm{sgn}(np), \tag{A16}$$

$$\mathcal{L}(n,p) = \frac{|n|}{R_2}\frac{\dot{b}}{2b}\left(\frac{(A_{12}R^{2|n|}-1)R^{|p|-|n|}}{A_{12}(1-R^{2|p|})}\right)\mathrm{sgn}(np), \tag{A17}$$

$$\mathcal{M}(n,p) = \frac{|n|}{R_2}\left(\frac{(A_{12}R^{2|n|}-1)R^{|p|-|n|}}{A_{12}(1-R^{2|p|})}\right)\mathrm{sgn}(np), \tag{A18}$$

where

$$g_3(p) = \frac{A_{12}-1}{A_{12}(1-R^{2|p|})}, \tag{A19}$$

and

$$g_4(n,p) = \frac{R^{2|p|}(1+A_{12}A_{23}R^{2|n|}) - (A_{23}+A_{12}R^{2|n|})}{A_{23}(1+A_{12}R^{2|n|})(R^{2|p|}-1)}. \tag{A20}$$

[1] P. G. Saffman and G. I. Taylor, The penetration of a fluid into a porous medium or Hele-Shaw cell containing a more viscous liquid, Proc. R. Soc. London A **245**, 312 (1958).

[2] L. Paterson, Radial fingering in a Hele-Shaw cell, J. Fluid Mech. **113**, 513 (1981).

[3] J. D. Chen, Growth of radial viscous fingers in a Hele-Shaw cell, J. Fluid Mech. **201**, 223 (1989).

[4] J. A. Miranda and M. Widom, Radial fingering in a Hele-Shaw cell: A weakly nonlinear analysis, Physica D **120**, 315 (1998).

[5] I. Bischofberger, R. Ramanchandran, and S. R. Nagel, An island of stability in a sea of fingers: Emergent global features of the viscous-flow instability, Soft Matter **11**, 7428 (2015).

[6] S. J. Jackson, D. Stevens, H. Power, and D. Giddings, A boundary element method for the solution of finite mobility ratio immiscible displacement in a Hele-Shaw cell, Int. J. Numer. Methods Fluids **78**, 521 (2015).

[7] R. M. Oliveira, B. Abedi, L. F. Santos, P. S. Câmara, P. R. S. Mendes, Similarity characteristics in the morphology of radial viscous fingers, Phys. Fluids **35**, 042114 (2023).

[8] For review papers on the Saffman-Taylor instability see, for instance, G. M. Homsy, Viscous fingering in porous media, Annu. Rev. Fluid Mech. **19**, 271 (1987); K. V. McCloud and J. V. Maher, Experimental perturbations to Saffman-Taylor flow, Phys. Rep. **260**, 139 (1995); J. Casademunt, Viscous fingering as a paradigm of interfacial pattern formation: Recent results and new challenges, Chaos **14**, 809 (2004).

[9] M. J. Shelley, F. Tian, and K. Wlodarski, Hele–Shaw flow and pattern formation in a time-dependent gap, Nonlinearity **10**, 1471 (1997).

[10] S. K. Thamida, P. V. Takhistov, and H.-C. Chang, Fractal dewetting of a viscous adhesive film between separating parallel plates, Phys. Fluids **13**, 2190 (2001).

[11] J. A. Miranda and R. M. Oliveira, Time-dependent gap Hele-Shaw cell with a ferrofluid: Evidence for an interfacial singularity inhibition by a magnetic field, Phys. Rev. E **69**, 066312 (2004).

[12] R. M. Oliveira and J. A. Miranda, Stretching of a confined ferrofluid: Influence of viscous stresses and magnetic field, Phys. Rev. E **73**, 036309 (2006).

[13] M. Ben Amar and D. Bonn, Fingering instabilities in adhesive failure, Physica D **209**, 1 (2005).

[14] A. Lindner, D. Derks, and M. J. Shelley, Stretch flow of thin layers of Newtonian liquids: Fingering patterns and lifting forces, Phys. Fluids **17**, 072107 (2005).

[15] J. Nase, D. Derks, and A. Lindner, Dynamic evolution of fingering patterns in a lifted Hele–Shaw cell, Phys. Fluids **23**, 123101 (2011).

[16] M. Zhao, Z. Niroobakhsh, J. Lowengrub, and S. Li, Nonlinear limiting dynamics of a shrinking interface in a Hele-Shaw cell, J. Fluid Mech. **910**, A41 (2021).

[17] A. Zosel, Adhesion and tack of polymers: Influence of mechanical properties and surface tensions, Colloid Polym. Sci. **263**, 541 (1985).

[18] H. Lakrout, P. Sergot, and C. Creton, Direct observation of cavitation and fibrillation in a probe tack experiment on model acrylic pressure-sensitive-adhesives, J. Adhes. **69**, 307 (1999).

[19] B. A. Francis and R. G. Horn, Apparatus-specific analysis of fluid adhesion measurements, J. Appl. Phys. **89**, 4167 (2001).

[20] D. Derks, A. Lindner, C. Creton, and D. Bonn, Cohesive failure of thin layers of soft model adhesives under tension, J. Appl. Phys. **93**, 1557 (2003).

[21] S. Poivet, F. Nallet, C. Gay, J. Teisseire, and P. Fabre, Force response of a viscous liquid in a probe-tack geometry: Fingering versus cavitation, Eur. Phys. J. E **15**, 97 (2004).

[22] S. Sinha, T. Dutta, and S. Tarafdar, Adhesion and fingering in the lifting Hele-Shaw cell: Role of the substrate, Eur. Phys. J. E **25**, 267 (2008).

[23] P. H. A. Anjos, E. O. Dias, L. Dias, and J. A. Miranda, Adhesion force in fluids: Effects of fingering, wetting, and viscous normal stresses, Phys. Rev. E **91**, 013003 (2015).

[24] P. H. A. Anjos, F. M. Rocha, and E. O. Dias, Controlling fluid adhesion force with electric fields, Phys. Rev. E **106**, 055109 (2022).

[25] H. Wahdat, C. Zhang, N. Chan, and A. J. Crosby, Pressurized interfacial failure of soft adhesives, Soft Matter **18**, 755 (2022).

[26] S. B. Gorell and G. M. Homsy, A theory of the optimal policy of oil recovery by secondary displacement processes, SIAM J. Appl. Math. **43**, 79 (1983).

[27] L. W. Lake, *Enhanced Oil Recovery* (Prentice Hall, Englewood Cliffs, NJ, 1989).

[28] L. Paterson, The implications of fingering in underground hydrogen storage, Int. J. Hydrog. Energy **8**, 53 (1983).

[29] M. Bai, K. Song, Y. Sun, M. He, Y. Li, and J. Sun, An overview of hydrogen underground storage technology and prospects in China, J. Pet. Sci. Eng. **124**, 132 (2014).

[30] D. Cherrak, E. Guernet, P. Cardot, C. Herrenknecht, and M. Czok, Viscous fingering: A systematic study of viscosity effects in methanol-isopropanol systems, Chromatographia **46**, 647 (1997).

[31] G. Rousseaux, A. De Wit, and M. Martin, Viscous fingering in packed chromatographic columns: Linear stability analysis, J. Chromatogr., A **1149**, 254 (2007).

[32] W. Xu, J. Wang, F. Ding, X. Chen, E. Nasybulin, Y. Zhang, and J.-G. Zhang, Lithium metal anodes for rechargeable batteries, Energy Environ. Sci. **7**, 513 (2014).

[33] Z. Li, H. Zhang, X. Sun, and Y. Yang, Mitigating interfacial instability in polymer electrolyte-based solid-state lithium metal batteries with 4 V cathodes, ACS Energy Lett. **5**, 3244 (2020).

[34] D. Pihler-Puzović, P. Illien, M. Heil, and A. Juel, Suppression of complex fingerlike patterns at the interface between air and a viscous fluid by elastic membranes, Phys. Rev. Lett. **108**, 074502 (2012).

[35] T. T. Al-Housseiny, I. C. Christov, and H. A. Stone, Two-phase fluid displacement and interfacial instabilities under elastic membranes, Phys. Rev. Lett. **111**, 034502 (2013).

[36] D. Pihler-Puzović, G. G. Peng, J. R. Lister, M. Heil, and A. Juel, Viscous fingering in radial elastic-walled Hele-Shaw cell, J. Fluid Mech. **849**, 163 (2018).

[37] T. T. Al-Housseiny and H. A. Stone, Controlling viscous fingering in tapered Hele-Shaw cells, Phys. Fluids **25**, 092102 (2013).

[38] S. J. Jackson, H. Power, D. Giddings, and D. Stevens, The stability of immiscible viscous fingering in Hele-Shaw cells with spatially varying permeability, Comput. Methods Appl. Mech. Eng. **320**, 606 (2017).

[39] G. Bongrand and P. A. Tsai, Manipulation of viscous fingering in a radially tapered cell geometry, Phys. Rev. E **97**, 061101(R) (2018).

[40] S. S. S. Cardoso and A. W. Woods, The formation of drops through viscous instability, J. Fluid Mech. **289**, 351 (1995).

[41] S. W. Li, J. S. Lowengrub, J. Fontana, and P. Palffy-Muhoray, Control of viscous fingering patterns in a radial Hele-Shaw cell, Phys. Rev. Lett. **102**, 174501 (2009).

[42] E. O. Dias, E. Alvarez-Lacalle, M. S. Carvalho, and J. A. Miranda, Minimization of viscous fluid fingering: A variational scheme for optimal flow rates, Phys. Rev. Lett. **109**, 144502 (2012).

[43] T. H. Beeson-Jones and A. W. Woods, Control of viscous instability by variation of injection rate in a fluid with time-dependent rheology, J. Fluid Mech. **829**, 214 (2017).
[44] L. C. Morrow, T. J. Moroney, and S. W. McCue, Numerical investigation of controlling interfacial instabilities in non-standard Hele-Shaw configurations, J. Fluid Mech. **877**, 1063 (2019).
[45] I. M. Coutinho and J. A. Miranda, Control of viscous fingering through variable injection rates and time-dependent viscosity fluids: Beyond the linear regime, Phys. Rev. E **102**, 063102 (2020).
[46] S. Gholinezhad, A. Kantzas, and S. L. Bryant, Control of interfacial instabilities through variable injection rate in a radial Hele-Shaw cell: A nonlinear approach for late-time analysis, Phys. Rev. E **107**, 065108 (2023).
[47] J. Kim, F. Xu, and S. Lee, Formation and destabilization of the particle band on the fluid-fluid interface, Phys. Rev. Lett. **118**, 074501 (2017).
[48] R. Luo, Y. Chen, and S. Lee, Particle-induced viscous fingering: Review and outlook, Phys. Rev. Fluids **3**, 110502 (2018).
[49] M. Mirzadeh and M. Z. Bazant, Electrokinetic control of viscous fingering, Phys. Rev. Lett. **119**, 174501 (2017).
[50] T. Gao, M. Mirzadeh, P. Bai, K. M. Conforti, and M. Z. Bazant, Active control of viscous fingering using electric fields, Nat. Commun. **10**, 4002 (2019).
[51] P. H. A. Anjos, M. Zhao, J. Lowengrub, and S. Li, Electrically controlled self-similar evolution of viscous fingering patterns, Phys. Rev. Fluids **7**, 053903 (2022).
[52] T. U. Islam and P. S. Gandhi, Viscous fingering in multiport Hele-Shaw cell for controlled shaping of fluids, Sci. Rep. **7**, 16602 (2017).
[53] S. D. Kanhurkar, V. Patankar, T. U. Islam, P. S. Gandhi, and A. Bhattacharya, Stability of viscous fingering in lifted Hele-Shaw cells with a hole, Phys. Rev. Fluids **4**, 094003 (2019).
[54] P. Karnal, Y. Wang, A. Jha, S. Gryska, C. Barrios, and J. Frechette, Interface stabilization in adhesion caused by elastohydrodynamic deformation, Phys. Rev. Lett. **131**, 138201 (2023).
[55] P. H. A. Anjos and S. Li, Weakly nonlinear analysis of the Saffman-Taylor problem in a radially spreading fluid annulus, Phys. Rev. Fluids **5**, 054002 (2020).
[56] P. O. S. Livera, P. H. A. Anjos, and J. A. Miranda, Magnetically induced interfacial instabilities in a ferrofluid annulus, Phys. Rev. E **104**, 065103 (2021).
[57] T. H. Beeson-Jones and A. W. Woods, On the selection of viscosity to suppress the Saffman–Taylor instability in a radially spreading annulus, J. Fluid Mech. **782**, 127 (2015).
[58] I. M. Coutinho and J. A. Miranda, Role of interfacial rheology on fingering instabilities in lifting Hele-Shaw flows, Phys. Rev. E **108**, 025104 (2023).
[59] S. Poivet, F. Nallet, C. Gay, and P. Fabre, Cavitation-induced force transition in confined viscous liquids under traction, Europhys. Lett. **62**, 244 (2003).
[60] E. O. Dias and J. A. Miranda, Effect of fluid inertia on probe-tack adhesion, Phys. Rev. E **85**, 016312 (2012).
[61] L. Kondic, M. J. Shelley, and P. Palffy-Muhoray, Non-Newtonian Hele-Shaw flow and the Saffman-Taylor instability, Phys. Rev. Lett. **80**, 1433 (1998).
[62] P. Fast, L. Kondic, M. J. Shelley, and P. Palffy-Muhoray, Pattern formation in non-Newtonian Hele–Shaw flow, Phys. Fluids **13**, 1191 (2001).
[63] T. Podgorski, M. C. Sostarecz, S. Zorman, and A. Belmonte, Fingering instabilities of a reactive micellar interface, Phys. Rev. E **76**, 016202 (2007).
[64] A. He, J. S. Lowengrub, and A. Belmonte, Modeling an elastic fingering instability in a reactive Hele-Shaw Flow, SIAM J. Appl. Math. **72**, 842 (2012).
[65] M. Zhao, A. Belmonte, S. Li, X. Li, and J. S. Lowengrub, Nonlinear simulations of elastic fingering in a Hele-Shaw cell, J. Comput. Appl. Math. **307**, 394 (2016).
[66] J. Li and H. Manikantan, Influence of interfacial rheology on viscous fingering, Phys. Rev. Fluids **6**, 074001 (2021).
[67] H. Conrado, E. O. Dias, and J. A. Miranda, Impact of interfacial rheology on finger tip splitting, Phys. Rev. E **107**, 015103 (2023).
[68] R. E. Rosensweig, *Ferrohydrodynamics* (Cambridge University Press, Cambridge, 1985).
[69] G. Bossis, S. Lacis, A. Meunier, and O. Volkova, Magnetorheological fluids, J. Magn. Magn. Mater. **252**, 224 (2002).
[70] J. de Vicente, D. J. Klingenbergb, and R. Hidalgo-Alvarez, Magnetorheological fluids: A review, Soft Matter **7**, 3701 (2011).